Experimental Thermal and Fluid Science 61 (2015) 48–58

Contents lists available at ScienceDirect

Experimental Thermal and Fluid Science

journal homepage: www.elsevier.com/locate/etfs

Isothermal velocity measurements in two HyperVapotron geometries using Particle Image Velocimetry (PIV)

A. Sergis [a,*], Y. Hardalupas [a], T.R. Barrett [b]

[a] The Department of Mechanical Engineering, Imperial College London, London SW7 2AZ, UK
[b] CCFE, Culham Science Centre, Abingdon, Oxfordshire OX14 3DB, UK

ARTICLE INFO

Article history:
Received 9 August 2014
Received in revised form 7 October 2014
Accepted 7 October 2014
Available online 27 October 2014

Keywords:
HyperVapotrons
Cooling
Fusion
Vapotron
PIV
Particle Image Velocimetry
High heat flux
HHF
HV
JET
MAST
DEMO

ABSTRACT

HyperVapotron beam stopping elements are high heat flux devices able to transfer large amounts of heat (of the order of 10–20 MW/m^2) efficiently and reliably making them strong candidates as plasma facing components for future nuclear fusion reactors or other applications where high heat flux transfer is required. They employ the Vapotron effect, a two phase complex heat transfer mechanism. The physics of operation of the device are not well understood and are believed to be strongly linked to the evolution of the flow fields of coolant flowing inside the grooves that form part of the design. An experimental study of the spatial and temporal behaviour of the flow field under isothermal conditions has been carried out on two replicas of HyperVapotron geometries taken from the Mega Amp Spherical Tokamak (MAST) and the Joint European Torus (JET) experiments. The models were tested under three isothermal operating conditions to collect coolant flow data and assess how the design and operational conditions might affect the thermal performance of the devices for single phase heat transfer. It was discovered that the in-groove speeds of MAST are lower and the flow structures less stable but less sensitive to free stream speed perturbations compared to the JET geometry. The MAST geometry was found to suffer from hydrodynamic end effects. A wake formation was discovered at the top of the groove entrance for the JET geometry, while this is absent from the MAST geometry. The wake does not affect significantly the mean operation of the device but it may affect the coolant pumping load of the device. For the JET variant, there is evidence that the typical operation with free stream flow speed of 6 m/s is advantageous.
© 2014 The Authors. Published by Elsevier Inc. This is an open access article under the CC BY license (http://creativecommons.org/licenses/by/3.0/).

1. Introduction

HyperVapotron (HV) beam stopping elements are durable, highly efficient two phase heat exchangers, which are able to withstand high heat fluxes (HHF), in excess of 10 MW/m^2, in steady state [1]. They were developed by Thomson CSF during the 1950s' to cool the anodes of high power tetrodes employed for communication purposes in klystron microwave tubes [1,2]. They have high geometric flexibility and can be moulded to the shape of the heat exchanging surface they are attached to. These factors make them viable for nuclear fusion applications as plasma facing components (PFC), hence their use in recent fusion reactor cooling studies. However, other conventional high heat flux transfer applications might also be benefited from their properties. HVs currently used are extensively on the Joint European Torus (JET) for all actively cooled neutral beam dumps and are being considered in the design of the next step international device, ITER (International Thermonuclear Experimental Reactor) and DEMO (DEMOnstration power plant) [1,3].

HVs consist of three main features. A high velocity free stream rectangular channel, which is joined over a substrate with grooves running perpendicular to the free stream flow, and a longitudinal groove running along each rib of the device (see Fig. 1). The device is oriented in a way that the grooved substrate is facing the oncoming heat flux. HVs employ the "Vapotron" effect – a complex, highly effective 2-phase heat transfer mode, which allows some parts of the device to operate with higher surface heat flux than the local critical heat flux (CHF) [4]. The operation of the device is characterised into three modes according to the heat flux received under given operating conditions (pressure and flow rate). These consist of a low power single phase heat transfer mode, an intermediate power 2-phase soft boiling regime mode and a high power hard boiling mode at which parts of the device (HHF facing wall) operate above the CHF point [1]. Irregular vortices form along the grooves, which appear to play an important role in the performance of the device. Upon the latter two modes of operation, at the onset of boiling, vapour bubbles form inside the grooves followed

* Corresponding author.
E-mail address: a.sergis09@imperial.ac.uk (A. Sergis).

http://dx.doi.org/10.1016/j.expthermflusci.2014.10.003
0894-1777/© 2014 The Authors. Published by Elsevier Inc.
This is an open access article under the CC BY license (http://creativecommons.org/licenses/by/3.0/).

by an injection of the vapour in the free stream, which then gets conveyed downstream and condenses.

In recent studies, various Computational Fluid Dynamics (CFD) and experimental work has been performed by research groups around the world to assess the applicability of HVs in fusion applications [1–26]. The experiments are generally focusing on the overall thermal performance of various geometries under various thermal loading scenarios and operating conditions, while the CFD studies in general try to recreate the experiments in an effort to model the operation of the device and hence be able to predict the thermal performance under expanded operation regimes and geometries without the need of further experimentation for design optimisation.

In the literature, only a handful of experimental and computational investigations provide information regarding the structure of the flow field inside a HyperVapotron. An experiment has been performed in the past [26] to provide qualitative information regarding the flow vortical structure observed in a single groove of a HV. However, this experiment remained a qualitative investigation and the data cannot be used to evaluate the corresponding CFD investigations that either followed or preceded it [4,23]. An experimental visualisation of the vapotron effect under all of the thermal power modes of operation has also been performed [5]. However, there is no detailed analysis of the recorded data to be able to evaluate the complex vaporisation, steam convection and condensation processes presented in the computational studies. The hydrodynamic flow structures evolving in the device have not been studied in detail experimentally and hence the physics of heat transfer, which are strongly related to the coolant flows, are not yet fully understood.

This paper is a significant expansion of our earlier work [27] and addresses the temporal behaviour of the isothermal flow field inside the grooves of a HV, which is important for the single phase heat transfer mode that initiates the 'Vapotron' effect during hot operation. This should enable a better understanding of both the design aspects and operation regimes of the device, as well as a better understanding of the initiation of the 'Vapotron' effect by analyzing the single phase heat transfer in the device before the vaporisation and ejection processes take place. Two geometries are investigated which relate to HV geometries found on JET and the Mega Amp Spherical Tokamak (MAST) [26] fusion facilities. Both geometries are evaluated under three operating conditions, which are defined by the free stream speed of the flow inside the devices, with one of them being the typical operating condition on both fusion experiments. The current paper builds on the preliminary results published in [27] by presenting a wide range of experimental results for a range of flow regimes. Quantitative temporal and spatial flow analysis is applied to the instantaneous measurements, including Proper Orthogonal Decomposition (POD) of the instantaneous flow distribution and image recognition of the instantaneous vortical centroid structure present inside the grooves of the HV. These results quantify the stability of the flow structures and evaluate consequences on the performance of the HV.

2. Methodology

2.1. Experimental rig

2.1.1. Test section

Two high optical quality transparent test sections were designed to model the JET and MAST related HV geometries (Fig. 2) [27]. The model is shortened to reduce experimental cost and complexity; it consists of five grooves. The choice of the number of grooves follows similar modelling principles as those found in other experimental modelling studies (i.e., at least three geometric repeats to deal with end effects when monitoring the middle one). This was also confirmed by the results of the experiment to follow.

The test sections were designed to have a well-conditioned, "top hat" inlet velocity profile by introducing flow straighteners and grids followed by a contraction with area ratio of 5 for the JET variant and 14 for the MAST variant inside the flow conditioning section of Fig. 3 upstream of the transparent test section. A diffuser was also added downstream of the test section to ensure that the downstream flow was also well conditioned. In addition, the operational scenarios tested and the experimental process followed required a high volumetric flow rate to be delivered at the test section with minimal vibrations. To achieve that, the rig was split into two main functional components, namely the pumping station and the measurements station, both connected into a closed circuit loop using flexible hoses. The pumping station comprises of a collection tank, a pump able to deliver volumetric flow rates up to 350 l/min, additional flow volumetric and pressure control vanes, electrical circuitry and pressure gauges to finely tune

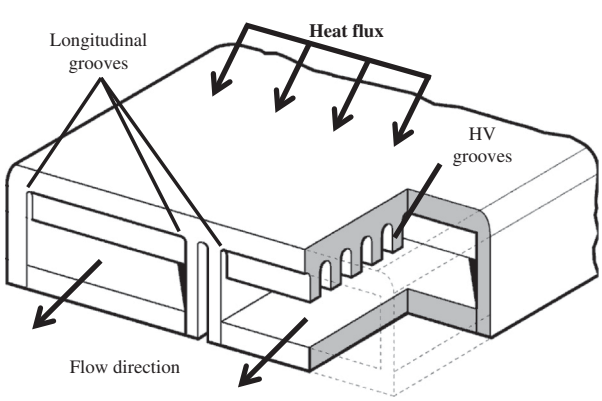

Fig. 1. Schematic of a complete HyperVapotron element with a cut out section revealing the transverse grooves.

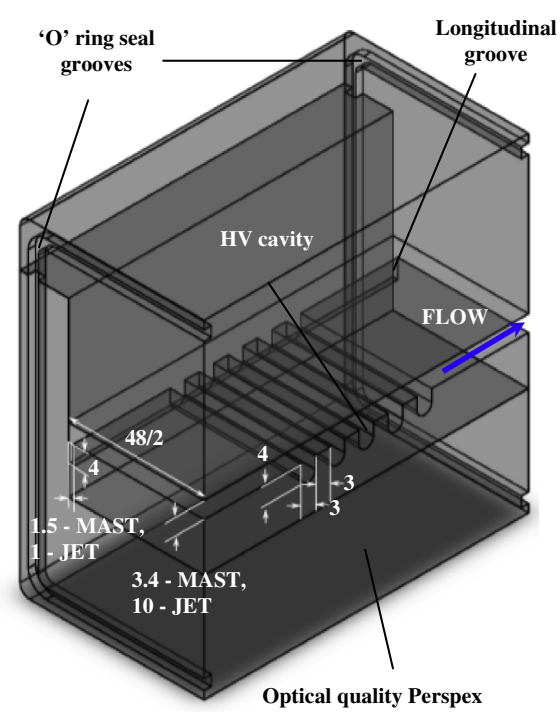

Fig. 2. Dimensionalised centre-line sectional view of the HV test sections under consideration. Dimensions are in mm.

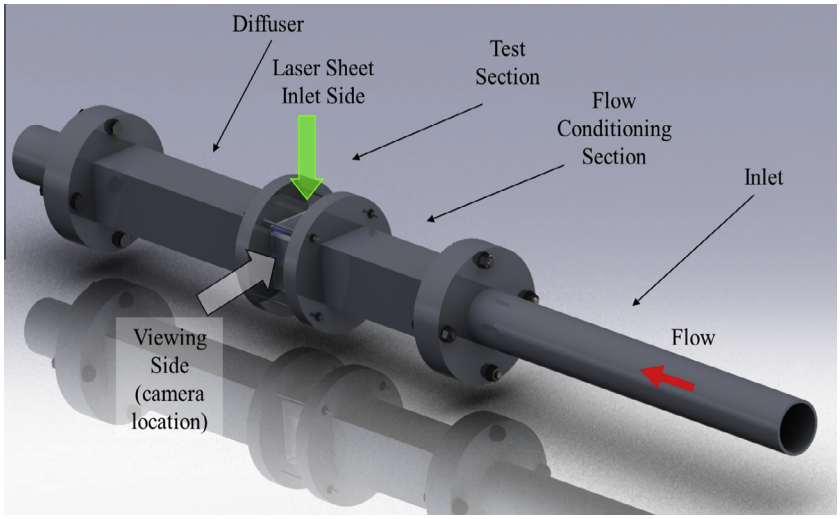

Fig. 3. Schematic of the experimental facility and optical access to the HyperVapotron test section.

and monitor the delivery of flow under the operational regimes tested.

2.1.2. Particle Image Velocimetry (PIV)

PIV is a well-established method for obtaining quantitative, high resolution flow visualisation data. The method relies on the use of a pulsed laser source to illuminate a thin sheet of tracers/seeders dispersed in the flow (a Litron Nano T PIV Nd-Yag laser was used) and a CCD camera (non-intensified LaVision Imager Intense camera with a resolution of 1376 × 1040 pixels) to record the tracer 'seeding' particles as they move inside the test section. A Nikkor 50 mm F/2.8 lens with manual focus was attached to the camera. Additionally, a 10 nm bandwidth 532 nm wavelength bandpass filter was attached to the lens to remove light wavelengths other than the one the laser produced and hence improve the image quality. The overall quantity of the flow 'seeding' particles is small to avoid changing the fluid properties of the working medium. A volumetric ratio of less than 0.0025% of tracers to water was used in this experiment. Al_2O_3 particles with 1 μm nominal diameter were used for 'seeding', which ensured appropriate tracking of the fluid flow for velocity measurements.

The laser pulses are a few nanoseconds long (7–9 ns) to avoid image "ghosting" and are emitted in pairs. The pulses inside a pair are separated by a few milliseconds. The time delay between the two pulses is adjusted in the range of 5–40 ms, according to the expected local flow velocity magnitude and is finely tuned by real time image analysis. 1000 pairs of images of the instantaneous flow were recorded for each operating scenario and geometry, in order to reduce the statistical uncertainties of the reported results. Each laser pulse pair is emitted at a rate of 1 Hz hence, in the time domain of the examined flow, each dataset collected from a pair of pulses is statistical independent from the rest and does not follow the evolutionary timescale of events taking place inside the device, since the timescale of the hydrodynamic events is shorter than the pulse pair separation time. The recorded images of the flow velocity field had real dimensions of 35.6 × 26.9 mm and the resulting spatial resolution was 30 μm. A section of the experimental rig with the optical access can be seen in Fig. 3.

Commercial software (LaVision DaVis 7.2) is used to process the recorded images and estimate the 'seeding' particle displacement, which is then translated into the fluid flow velocity. Initially, a shift and intensity correction routine is followed to stabilise the raw images and normalise the intensities of scattered light recorded. A cross correlation method was then used at which the interrogation window followed a multi pass refinement process from 512 × 512 pixels down to 8 × 8 pixels with an overlap of 50% to calculate the vector field. A multi pass post processing is then followed at which the quality of the first calculation is evaluated and filters are successively and repeatedly applied to remove noise and improve the accuracy of the calculation. Three filtering processes are followed. The first deletes vectors at which their cross correlation function peak ratio is less than a given value. Secondly a median filter is applied to strongly remove and iteratively replace vectors at which their RMS difference with their neighbouring vectors is larger than a value of the average RMS value of the neighbouring vectors. Vector groups can be removed with this process and replaced by interpolated ones. A smoothing filter is finally applied to improve the accuracy of the vector distribution. Multiple passes of these filters are applied with variable filtering parameters. At the final pass velocity vectors with a cross correlation function peak ratio of less than 3 are deleted. The median filter will also delete vectors at which their value is more than twice the RMS value of their neighbouring vectors. Groups of a maximum of 20 vectors can be removed and replaced by interpolated ones. Finally, a smoothing filter of 3 × 3 pixels is applied. The sample vector yield is close to 100%. Please note that the jagged processed velocity vector fields (particularly at the bottom of the grooves), as presented in this paper, do not correspond to a geometrical feature of the actual test section but arise from the limitation of the processing software to provide a high resolution curved boundary definition between the liquid and the solid walls.

The distributions of the mean flow velocity and the standard deviation of the corresponding flow velocity fluctuations were estimated from the instantaneous flow velocity images. These averaged quantities were based on 1000 statistical independent samples, which led to statistical uncertainties of the order of ±2.2% and ±3.2% for the temporal and spatial mean of JET and MAST respectively within a 95% confidence level.

2.2. Further processing of PIV results

2.2.1. Proper Orthogonal Decomposition

Proper Orthogonal Decomposition (POD) is the mechanical engineering equivalent of Principal Component Analysis (PCA) in mathematics. It is a multivariate eigenvector based analysis at which an orthogonal transformation is used to decompose series of correlated velocity data, recorded by each laser pulse pair, into a set of uncorrelated components/modes (Eigen-components/

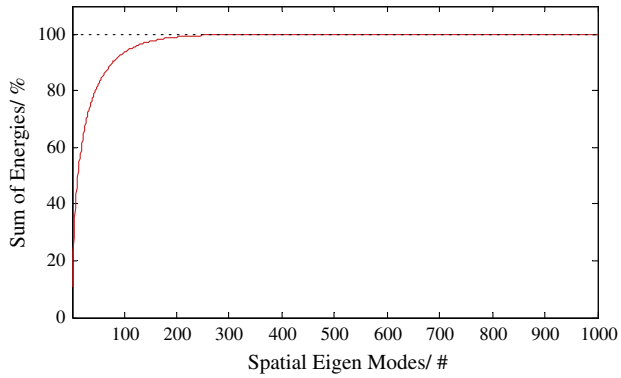

Fig. 4. Sum of energies of the spatial Eigen modes for JET geometry at a free stream speed of 10 m/s.

modes each orthogonal to the next). The components are given an "energy level", namely a weighing factor towards their contribution to the correlated series. The higher the energy level the higher the effect of a particular Eigen-mode to the overall average of the series. The Eigen-components are presented in a series with the same number count as the total dataset number used; the first being the most energetic and the last being the least energetic. The decomposition images produced have the mean flow of the entire series subtracted, so as to be able to get a clearer view of the fluctuating flow components. Fig. 4 shows an example of the energy contribution of the different eigenmodes to the flowfield.

Commercial software (LaVision DaVis 7.2) was used to decompose the velocity data series for each geometry and for each operational condition tested. The decomposed velocity field is used to understand better which instantaneous flow structures are more influential for the operation of the device. The data can be used to analyse how the design and operation of the flow geometry affects the formation of the instantaneous vortical structures. The analysis was focused on the flow field of the middle groove of each of the flow geometries, as it is expected to be more representative for the flow inside the majority of the multiple grooves present inside a real device, which may not be strongly influenced by hydrodynamic end effects.

2.2.2. Image recognition routines

Due to the large number of recorded images, additional routines were developed so as to automatically analyse the local characteristics of the vortices inside the grooves of each test section as well as to detect a breakup of an instantaneous vortical structure. The

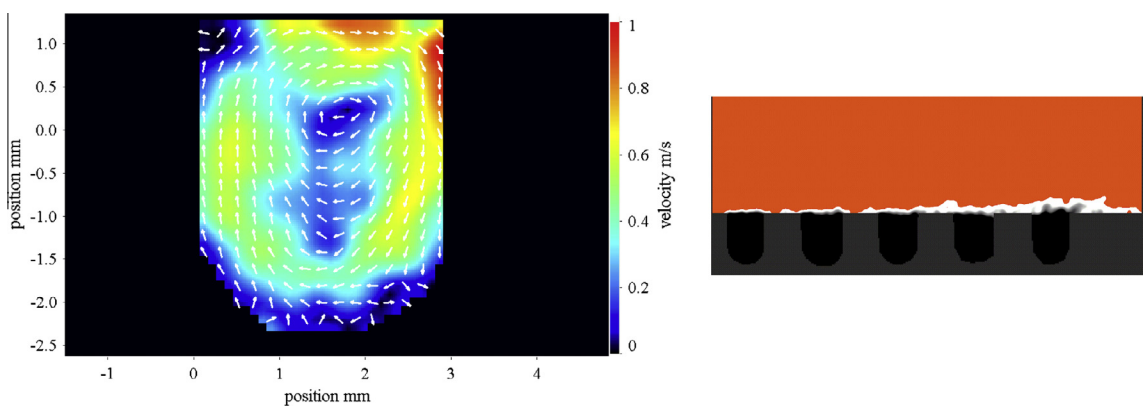

Fig. 5. Instantaneous example image of the velocity vector field inside the middle groove identifying a vortical structure (on the left) and a view of the entire test section with the wake formation highlighted in the free stream on top of the grooves (on the right). The white highlighted region in the right hand side image represents the velocity field region where the velocity magnitude is less than the bulk average of the free stream region. Both instantaneous images are under a 3 m/s target free stream speed in the JET geometry.

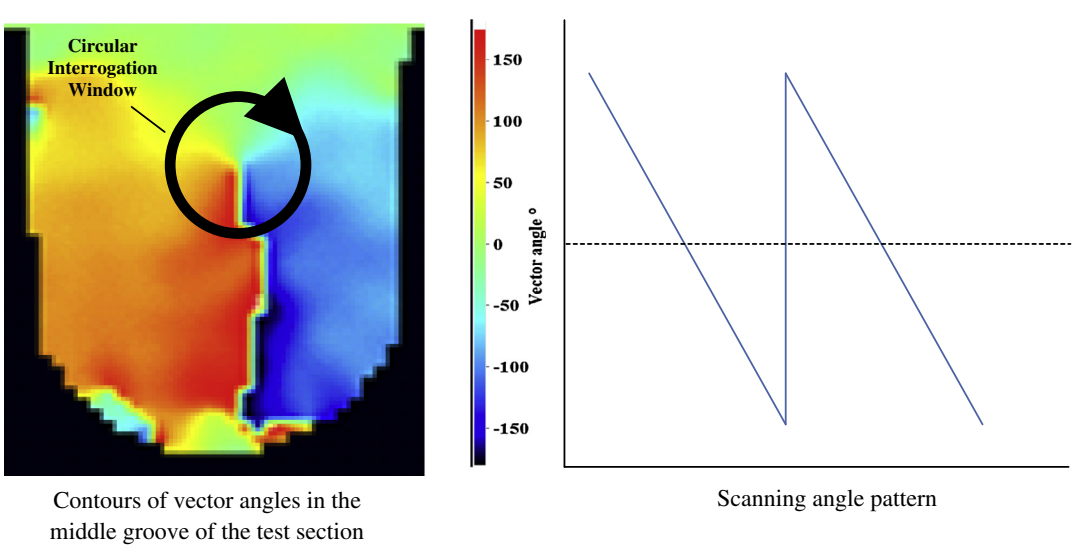

Fig. 6. Schematic of the recognition logic of the centroid of a vortical flow structure.

routines also investigate possible evolution of wakes at the entrance of the grooves inside the free stream channel and assess how these might affect the locational and formational stability of the vortical structures inside the grooves. The challenge of forming the data processing routines was not straightforward as the high irregularity of both the vortical structures and the wake made it impossible to use traditional methods of detection of the fluid quantities (see Fig. 5) such as vorticity and turbulence intensity filters. The right hand image of Fig. 5 shows the instantaneous flow behaviour in the free stream above the 5 grooves of the test section. The white contours on the image highlight the regions where the fluid velocity is lower than the bulk average for the region. It should be noted that the free stream flow above the grooves varies significantly and is affected by the stability of the vortical structures within the grooves, which will be quantified below. Averaging methods and interrogation windows had to be formed to be able to resolve the instantaneous flow features.

The routines for the detection of wake presence in the freestream flow are formed in a way to automatically register the presence of a flow disturbance in the free stream and mark the corresponding groove number that is located below it for every data set. The routine then loads a PIV processed matrix, which contains the values of flow velocity with a resolution of 30 μm for the entire viewing area. The code then makes use of rectangular overlapping interrogation windows and scans the full length of the free stream area closer to the groove openings at which the flow wake is formed. An average speed is calculated for every interrogation window and compared to the next. If the average speed in the window is less than 80% of the target free stream velocity (a threshold that has been defined by studying the wake attributes) the interrogation window is flagged. If the flagged windows span a continuous distance of more than two groove widths (namely if a wake is long enough to affect the flow in more than one groove) then the routine identifies a wake and the corresponding grooves of the dataset are marked. The wake formation and its extent aids to understand better the interaction between the flow inside the grooves and the freestream by identifying the conditions of a wake presence and how this wake correlates with the instantaneous and average behaviour of the flow inside the grooves.

The routine for the detection of the locational stability of the vortical structures inside the grooves required advanced methods of image recognition to increase the sensitivity of the detection of the vortex centroid, while accommodating large irregularities in its shape. The geometrical irregularity of the vortex formation makes it impossible to use traditional flow quantities, such as the flow vorticity, to detect the vortex centroid. Alternative image analysis routines had to be devised that recognised vortical patterns according to a relative size and morphology and allowed a large degree of vortex formation irregularity. The vector angles of the fluid packets forming a vortical structure are examined. A matrix from each dataset containing the velocity vector angles at a resolution of 30 μm is used. A fixed pattern is observed close to the vortex centroid at which the average vector angle is decreasing and a "jump" is detected when a clockwise circular scanning is completed, as seen in Fig. 6.

The morphological features of a vortex described by a velocity vector angle plot (such as the one in Fig. 6) contain distinctive features; the pattern followed by the vector angles, as described earlier, and a "dead" undefined region of vector angles which are located inside the vortex "eye". Taking account of these features and allowing for irregularities, an elaborate design for the interrogation window is required (Fig. 7). An averaging process is applied to calculate the average velocity vector angle in successive quadrants at a time of the interrogation window bounded by the external radius (R_{ext}) and internal radius (R_{int}) of the interrogation window (hatched area in Fig. 7). The internal radius corresponds to

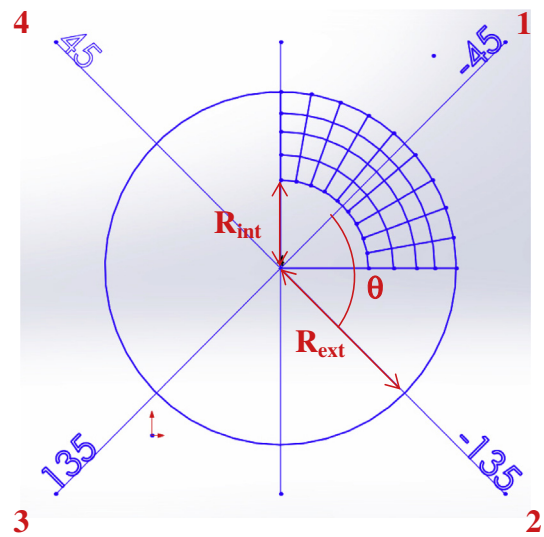

Fig. 7. Circular interrogation window with polar coordinates of the average sector angles.

the characteristic size of the eye of the vortex, while the external radius represents an average characteristic size of the vortices to be recognised (this plays an important role in the overall locational accuracy of the calculated vortex centroid). If the vortex had a geometrically perfect circular shape, the average vector angle from successive quatrands (θ) would have been in steps of 90°. Allowing for irregularities though, θ can be reduced to allow deformed and skewed vortices to be detected.

The comparison starts from quadrant "1" and ends in quadrant "1" hence making in total four angle comparisons. The interrogation window scans the entire area of the grooves searching for the vortex velocity vector angle pattern and returns the locations when this criterion is satisfied. Control criteria are in place to abort a scanning if the pattern is quickly found to be missing from the interrogation window (this can happen as soon as the scanning is completed inside the 2nd quantrant and onwards) hence improving computational efficiency. The circular interrogation windows are overlapped to increase the accuracy of the calculation. The overlap distance is as small as 1/10th of R_{ext}. To accommodate different vortex sizes, a generally large R_{ext} is used (between 0.25 and 0.5 mm) in order to capture vortices with a characteristic size ranging between 0.5 and 1 mm in diameter. This increases the locational accuracy of vortex detection away from the walls of the groove. However, it is nearly impossible to identify small vortices near the walls of the grooves. A "trial and error" process indicated a suitable value for R_{ext} which ensures a large overall accuracy. When a pattern is identified, the centre of the interrogation window is logged. As soon as the entire groove is scanned, a collection of points is attained for which the interrogation window has detected a centroid pattern. The geometrical centre of the entire

Table 1
Uncertainties in setting up target flow rates.

Geometry	Target free stream speed (m/s)	Target volumetric flow rate (l/min)	Flow metre uncertainty (%)
JET	3	88	4
	6	176	4
	10	293	3
MAST	3	32	6
	6	63	5
	10	105	4

Table 2
Measured normalised speed characteristics. Normalisation is by the free stream speed.

Free Stream Speed/ ms^{-1}	JET				MAST			
	$\langle\lvert\overline{\boldsymbol{V}}\rvert\rangle$	$\langle\lvert\overline{\boldsymbol{V}'}\rvert\rangle$	$\langle\lvert\overline{\boldsymbol{V}'_{REL}}\rvert\rangle$ (%)	Vortex Breakup Occurrences (%)	$\langle\lvert\overline{\boldsymbol{V}}\rvert\rangle$	$\langle\lvert\overline{\boldsymbol{V}'}\rvert\rangle$	$\langle\lvert\overline{\boldsymbol{V}'_{REL}}\rvert\rangle$ (%)	Vortex Breakup Occurrences (%)
3	0.118989	0.045314	38.1	2.6	0.110381	0.058569	53.1	9.7
6	0.122133	0.041868	34.3	2.4	0.094863	0.048105	50.7	7.0
10	0.120528	0.042246	35.1	4.7	0.085252	0.044969	52.7	7.8

Table 3
Comparison of measured normalised speed characteristics with those for the typical operating conditions (6 m/s freestream) given as percentage changes.

Free stream speed (ms^{-1})	JET				MAST			
	$\Delta\langle\lvert\overline{\boldsymbol{V}}\rvert\rangle$ (%)	$\Delta\langle\lvert\overline{\boldsymbol{V}'}\rvert\rangle$ (%)	$\Delta\langle\lvert\overline{\boldsymbol{V}'_{REL}}\rvert\rangle$ (%)	ΔVortex breakup occurrences (%)	$\Delta\langle\lvert\overline{\boldsymbol{V}}\rvert\rangle$ (%)	$\Delta\langle\lvert\overline{\boldsymbol{V}'}\rvert\rangle$ (%)	$\Delta\langle\lvert\overline{\boldsymbol{V}'_{REL}}\rvert\rangle$ (%)	ΔVortex breakup occurrences (%)
3	−2.6	8.2	3.8	0.2	16.4	21.8	2.4	2.7
10	−1.3	0.9	0.8	2.3	−10.1	−6.5	2.0	0.8

collection of points is calculated, which yields a good approximation of the vortex real centroid (accuracy is better than 500 μm).

3. Results and discussion

The results related to the velocity field are presented normalised by the corresponding free stream velocity for each condition. The related uncertainties in setting the flow rates are given by Table 1. The tabular results of Table 2 represent the averaged temporal and spatial quantities of the middle groove while the data in Table 3 represent its averaged temporal quantities. The velocity and POD field analysis study was focused on the 3rd groove, which is expected to be the least affected by hydrodynamic end effects. The POD presents the first four Eigen modes of the decomposition as there are no distinguishable features to extract from the fifth mode and onwards. An example of the Eigen mode energy levels for the JET HV at an operating free stream velocity of 10 m/s can be seen in Fig. 4. Similar energy levels were observed for the rest of the operational points and the MAST HV. The vortex locational analysis was extended to include both the entire section as well as the middle groove (3rd groove) in more detail. The investigation was one dimensional and the results took account of the locational coordinate perpendicular to the free stream flow. The wake interaction study took account of the entire test section only. Note that on Tables 2, 3 and 4 and Figs. 7–10, the following notation is used: $\langle\lvert\overline{\boldsymbol{V}}\rvert\rangle$ Groove spatially averaged normalised speed, $\langle\lvert\overline{\boldsymbol{V}'}\rvert\rangle$ Groove spatially averaged RMS of normalised velocity fluctuations and $\langle\lvert\overline{\boldsymbol{V}'_{REL}}\rvert\rangle$ Groove spatially averaged RMS of normalised velocity fluctuations further normalised by $\langle\lvert\overline{\boldsymbol{V}}\rvert\rangle$).

3.1. JET related HyperVapotron Geometry

3.1.1. Velocity fields

The normalised tabular data for the velocity fields and breakup occurrences of the vortex for the 3rd groove of the JET test section can be found in Table 2 while a comparison of the various operating conditions with those typically used in operational HV devices (free stream speed of 6 m/s) is provided in Table 3 (percentage differences). There is no significant change (<10%) in the non-dimensional (ND) groove speeds observed with higher or lower velocities than the typical operating conditions (free stream velocity of 6 m/s). The ND temporal and spatial averaged speeds appear to be lower for the 3 m/s and 10 m/s cases compared to the 6 m/s (by 3% and 1% respectively). The RMS values for the 3 m/s and 10 m/s cases are higher by 8% and 1% compared to the 6 m/s case. This is a useful result, and is evidence that the 6 m/s flow speed used in typical operation should be continued. The relative RMS of velocity fluctuations for the 3 m/s and 10 m/s cases also appear to be higher by 4% and 1% respectively compared to the 6 m/s case. The breakup occurrences of the vortex for the 3 m/s, 6 m/s and 10 m/s were small and limited to below 5% (3%, 2% and 5% respectively). It appears that the operation of the geometry at 3 m/s, 6 m/s and 10 m/s is similar in this respect.

Table 4
Comparison of the measured normalised speed characteristics of the MAST and JET geometries given as percentage changes.

Free stream speed (ms^{-1})	MAST			
	$\Delta\langle\lvert\overline{\boldsymbol{V}}\rvert\rangle$ (%)	$\Delta\langle\lvert\overline{\boldsymbol{V}'}\rvert\rangle$ (%)	$\Delta\langle\lvert\overline{\boldsymbol{V}'_{REL}}\rvert\rangle$ (%)	ΔVortex breakup occurrences (%)
3	−17.9	14.4	15.0	1.7
6	−30.3	3.1	16.4	3.0
10	−35.4	−2.9	17.7	3.3

There is no significant change of the groove vortex morphology for the 6 m/s and 10 m/s cases as seen in Fig. 9. The vortex appears to have higher velocity gradients close to the side walls and lower close to the bottom boundary. The ND average velocity for operating conditions of 3 m/s shows a slightly increased ND speed close to the right boundary. The RMS plots are similar for all three cases

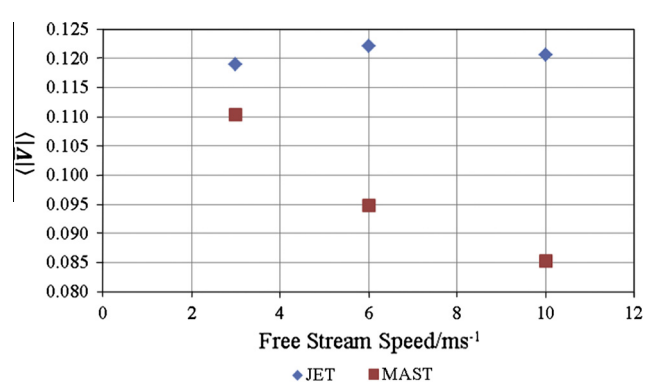

Fig. 8. Comparison of the JET and MAST in groove mean normalised flow speeds vs. free stream speed.

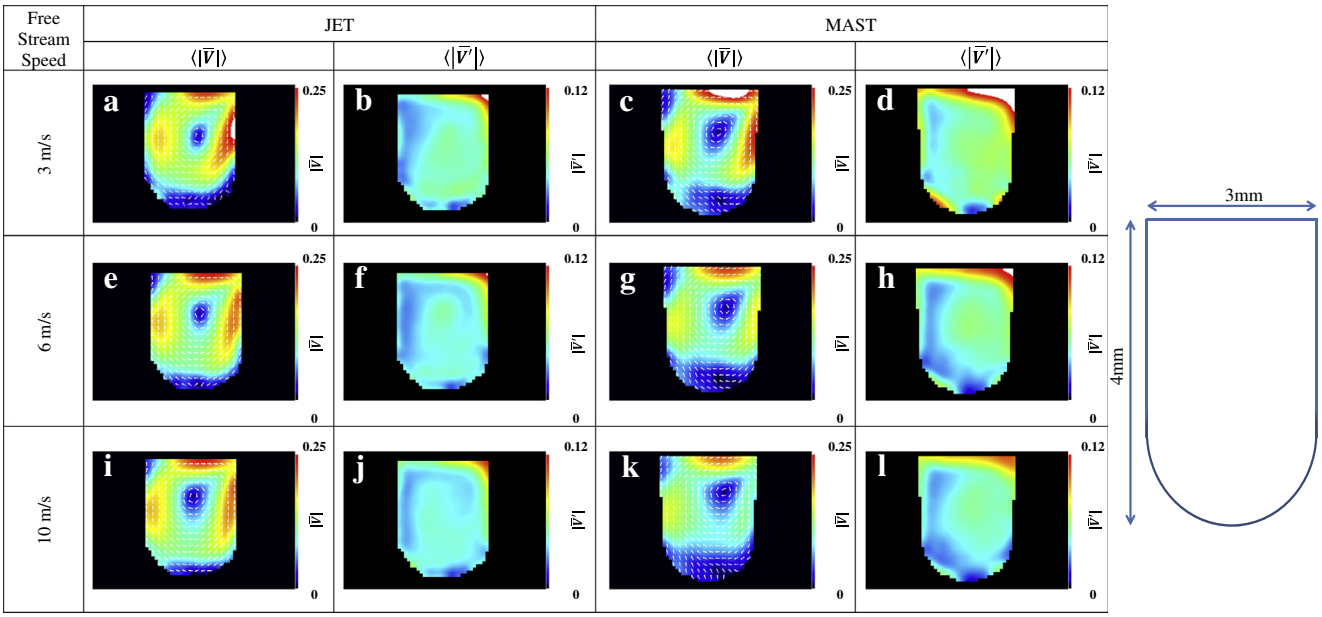

Fig. 9. Mean normalised velocity and RMS of normalised velocity fluctuations for the JET and MAST geometries. Normalisation is by the free stream speed.

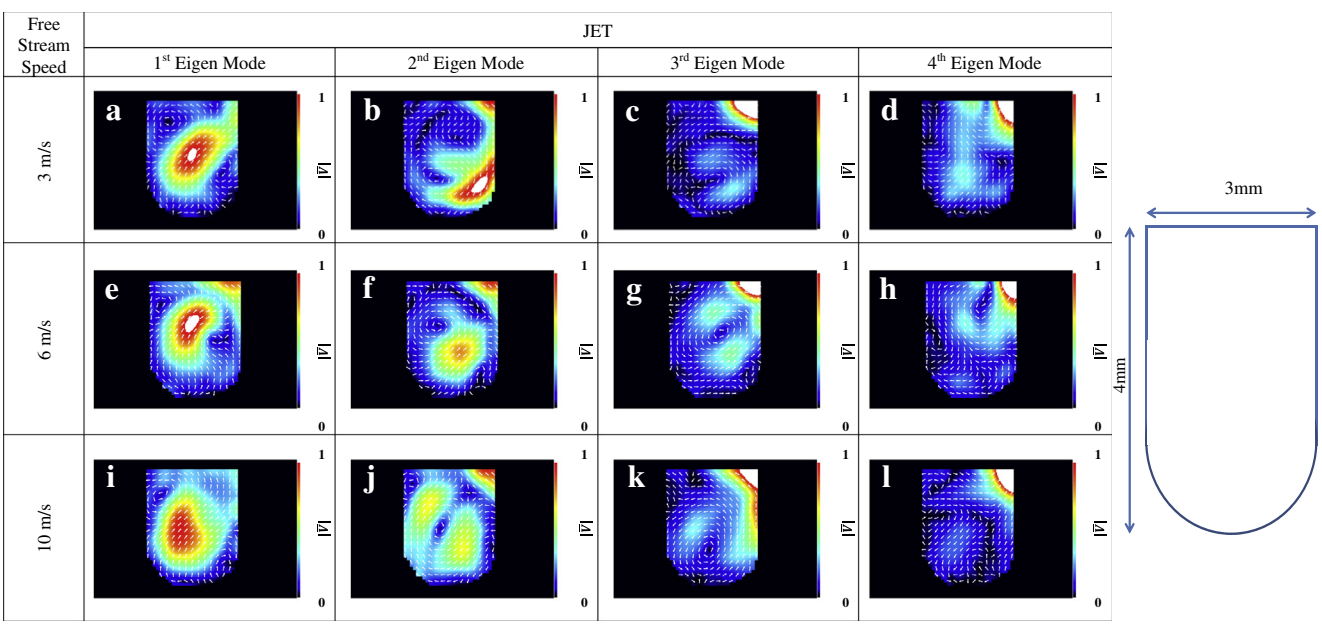

Fig. 10. POD analysis of the flow field inside the central groove showing the first four most energetic Eigen modes of the normalised velocity fields for the JET geometry. Normalisation is by the free stream speed.

with a minor exception of the right top corner for the 10 m/s case which appears to have an overall lower RMS value than the rest.

3.1.2. Proper Orthogonal Decomposition (POD) analysis

The POD Eigen modes for JET can be found in Fig. 10. The first Eigen mode shows the effects of the separation vortex occurring at the left top corner of the groove with a strong diagonal flow in the middle of the groove and a secondary vortex at the lower right section of the groove (the Eigen mode energy levels are 8%, 9% and 7% for the 3 m/s, 6 m/s and 10 m/s cases respectively). The effects of these features (size of vortices and diagonal flow) decrease with increasing free stream velocity. The 2nd to 4th Eigen modes do not provide any additional information regarding the flow field.

3.1.3. Groove Vortex locational characterisation

Fig. 12 contains the characterisation of the vortex centroid location in the groove. The vortex in the third groove appears to be stabilised around its average position for all three cases with the probability that the centroid remains around its average temporal position (within a 0.5 mm bounded area above and below the mean average centroid) being around 95–96%. Upon deviation from the temporal equilibrium position, the vortex is statistically more probable to be situated near the lower boundary

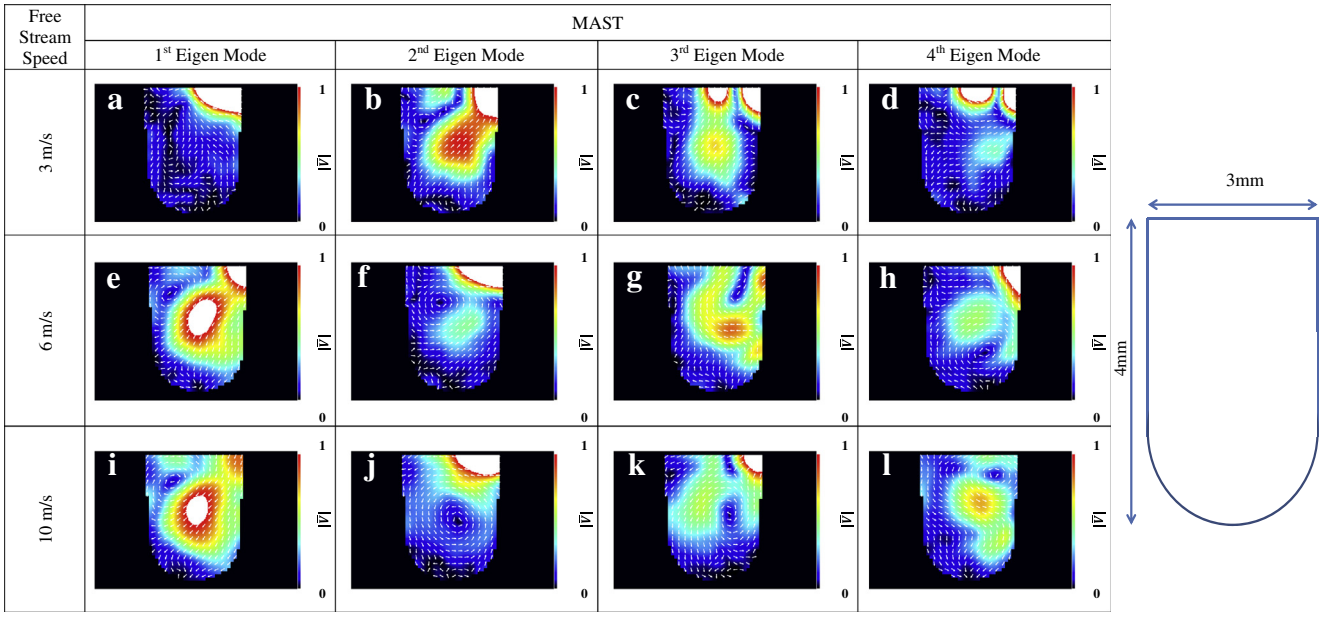

Fig. 11. POD analysis of the flow field inside the central groove showing the first four most energetic Eigen modes of the normalised velocity fields for the MAST geometry. Normalisation is by the free stream speed.

Geometry	Speed/ (m/s)	Groove No	Centroid Position															
			Counts								Statistics							
			Entire Section				Single Groove				Entire Section				Single Groove			
			Low	Average	High	No Vortex	Low	Average	High	No Vortex	Low	Average	High	No Vortex	Low	Average	High	No Vortex
JET	3	1	138	818	26	18	13	955	6	26	0.138	0.818	0.026	0.018	0.013	0.955	0.006	0.026
		2	33	736	221	10					0.033	0.736	0.221	0.010				
		3	15	959	4	22					0.015	0.959	0.004	0.022				
		4	18	955	4	23					0.018	0.955	0.004	0.023				
		5	32	912	18	38					0.032	0.912	0.018	0.038				
		Total	236	4380	273	111					0.047	0.876	0.055	0.022				
	6	1	11	934	19	36	10	964	2	24	0.011	0.934	0.019	0.036	0.010	0.964	0.002	0.024
		2	13	970	7	10					0.013	0.970	0.007	0.010				
		3	21	963	2	14					0.021	0.963	0.002	0.014				
		4	5	965	1	29					0.005	0.965	0.001	0.029				
		5	9	946	8	37					0.009	0.946	0.008	0.037				
		Total	59	4778	37	126					0.012	0.956	0.007	0.025				
	10	1	18	890	20	72	1	950	2	47	0.018	0.890	0.020	0.072	0.001	0.950	0.002	0.047
		2	13	972	10	5					0.013	0.972	0.010	0.005				
		3	10	943	0	47					0.010	0.943	0.000	0.047				
		4	5	924	0	71					0.005	0.924	0.000	0.071				
		5	10	966	2	22					0.010	0.966	0.002	0.022				
		Total	56	4695	32	217					0.011	0.939	0.006	0.043				
MAST	3	1	No established vortex				26	863	14	97	No established vortex				0.026	0.863	0.014	0.097
		2	176	704	41	79					0.176	0.704	0.041	0.079				
		3	31	898	27	44					0.031	0.898	0.027	0.044				
		4	65	858	19	58					0.065	0.858	0.019	0.058				
		5	33	863	45	59					0.033	0.863	0.045	0.059				
		Total	305	3610	837	248					0.061	0.722	0.167	0.050				
	6	1	403	498	49	50	37	885	8	70	0.403	0.498	0.049	0.050	0.037	0.885	0.008	0.070
		2	48	885	12	55					0.048	0.885	0.012	0.055				
		3	51	887	9	53					0.051	0.887	0.009	0.053				
		4	22	949	9	20					0.022	0.949	0.009	0.020				
		5	51	823	83	43					0.051	0.823	0.083	0.043				
		Total	575	4042	162	221					0.115	0.808	0.032	0.044				
	10	1	176	651	47	126	24	883	15	78	0.176	0.651	0.047	0.126	0.024	0.883	0.015	0.078
		2	119	807	30	44					0.119	0.807	0.030	0.044				
		3	25	908	13	54					0.025	0.908	0.013	0.054				
		4	10	964	2	24					0.010	0.964	0.002	0.024				
		5	57	783	94	66					0.057	0.783	0.094	0.066				
		Total	387	4113	186	314					0.077	0.823	0.037	0.063				

Fig. 12. Vortex centroid locational stability analysis.

of the groove compared to the higher boundary. The probability of the vortex centroid location remaining around its temporal average position decreases marginally with increasing free stream velocity. The vortex locational stability appears to be larger for the 6 m/s case.

A similar picture is presented by the overall groove vortex characterisations in grooves one to five with the overall section exhibiting vortex stabilisation about its temporal equilibrium position with a probability ranging from 88–96%.

3.1.4. Wake interactions with vortices

Fig. 13 contains the vortex centroid locational characterisation for the entire test section in the presence of wake in the free stream. There is wake formation at the free stream channel

boundary at the top side of the grooves for the JET geometry. The instantaneous wake can grow to occupy up to about 10–15% of the free stream channel height. The wake probability occurrence is large for the JET and follows a decreasing trend for an increasing free stream velocity (67%, 43% and 34% for the 3 m/s, 6 m/s and 9 m/s respectively). The wake is most probable to start from the upstream groove and conveyed downstream. The probability of the existence of a wake on top of the downstream grooves follows an increasing trend.

The wake has negligible effect on the overall vortex breakup occurrences for the entire section. It is also found to induce minor (below 10%) vortex centroid stabilisation around its average position due to the lower groove opening free stream velocities, which "shield" the groove from free stream perturbations. The fact that the probability of the wake formation decreases with increasing free stream speed is owing to the increased shear stresses, which act as a dampening parameter to free stream irregularities.

3.2. MAST related HyperVapotron Geometry

3.2.1. Velocity fields

The normalised tabular data for the velocity fields and breakup occurrences of the vortex for the 3rd groove of the MAST test section can be found in Table 2, while a comparison of the various operating conditions with the typical HV flow (free stream speed of 6 m/s) is provided in Table 3 (percentage differences). There is moderate change in the ND average groove speeds compared to the current operating conditions. The average ND groove speed at 3 m/s is by 16% higher and, at the 10 m/s case, 10% lower compared to the normal operating conditions (free stream of 6 m/s). This indicates an overall average groove speed reduction with the increase of the free stream velocity. There is significant change on the ND RMS value for 3 m/s (an increase of around 22%), while, for the 10 m/s, there is a decrease of 7% compared to the 6 m/s case. The relative RMS values appear to be small with an increase of 2% for both free stream speeds, compared to the operating conditions. The vortex breakup occurrences seem to remain the same for higher or lower free stream speeds in between 7% and 10% (10%, 7% and 8% for the 3 m/s, 6 m/s and 10 m/s respectively). The operation of the MAST geometry is affected significantly by changing the free stream velocity. It is not clear why this geometry performs differently in the three flow regimes compared to the JET design. This highlights the sensitivity of the device performance to the internal geometry and underlines the need to understand and predict their performance.

There is no significant change of the groove vortex morphology (see Fig. 9) for the 6 m/s and 10 m/s cases. The vortex appears to have higher velocity gradients on the side walls and lower on the bottom boundary. The 3 m/s ND average velocity plot shows a slightly increased ND speed on the top boundary. The RMS plots are similar for all three cases with the exception of the right top corner of the 3 m/s case, where the RMS values appear higher.

3.2.2. Proper Orthogonal Decomposition (POD) analysis

The first four POD Eigen modes for MAST can be found in Fig. 11. A separation vortex and diagonal middle flow appear to be present for only the 6 m/s and 10 m/s cases as seen from the 1st and 2nd Eigen modes. The energy levels of the 1st Eigen modes are 10%, 13% and 13% for the 3 m/s, 6 m/s and 10 m/s cases respectively. For subsequent Eigen modes the energies reduce significantly. It appears that the narrower channel height suppresses the separation vortex for low free stream velocities. Subsequent Eigen modes provide little additional information compared to the mean flow.

3.2.3. Groove Vortex locational characterisation

Fig. 12 contains the analysis of the vortex centroid locational characterisation. The vortex, similarly to the JET geometry, appears to be stabilised around its average temporal position for all three cases with the probability that the centroid being around its average position (within a 0.5 mm bounded area above and below the average centroid) being around 86–88%. Upon deviation from the temporal equilibrium position, the MAST vortex is statistically more probable to be near the lower boundary of the groove compared to the higher boundary. The probability of the vortex centroid location being around its average temporal position remains about the same with increasing free stream velocity.

A similar behaviour is presented by the overall groove vortex characterisation in grooves one to five with the overall section

Geometry	Speed/ (m/s)	Groove No	Centroid Position								
			Counts				Statistics				
			Entire Section				Entire Section				
			Low	Average	High	No Vortex	Low	Average	High	No Vortex	Wake Presence
JET	3	1	0	0	0	0	0.000	0.000	0.000	0.000	0.000
		2	0	6	5	0	0.000	0.545	0.455	0.000	0.011
		3	2	84	0	3	0.022	0.944	0.000	0.034	0.089
		4	8	222	1	3	0.034	0.949	0.004	0.013	0.234
		5	7	306	7	15	0.021	0.913	0.021	0.045	0.335
		Total	17	618	13	21	0.025	0.924	0.019	0.031	0.669
	6	1	0	0	0	0	0.000	0.000	0.000	0.000	0.000
		2	0	7	0	0	0.000	1.000	0.000	0.000	0.007
		3	1	58	0	1	0.017	0.967	0.000	0.017	0.060
		4	1	133	0	4	0.007	0.964	0.000	0.029	0.138
		5	1	217	1	9	0.004	0.952	0.004	0.039	0.228
		Total	3	415	1	14	0.007	0.958	0.002	0.032	0.433
	10	1	0	0	0	0	0.000	0.000	0.000	0.000	0.000
		2	0	6	0	0	0.000	1.000	0.000	0.000	0.006
		3	0	34	0	3	0.000	0.919	0.000	0.081	0.037
		4	1	97	0	11	0.009	0.890	0.000	0.101	0.109
		5	0	184	0	7	0.000	0.963	0.000	0.037	0.191
		Total	1	321	0	21	0.003	0.936	0.000	0.061	0.343

Fig. 13. Vortex centroid locational stability analysis with wake formation.

exhibiting vortex stabilisation about its temporal equilibrium position with a probability ranging from 72% to 82%.

3.2.4. Wake interactions with vortex

No wake was formed in the MAST geometry due to the higher shear stresses encountered in the free stream section, which act to suppress the free stream non-uniformities.

3.3. Comparison of the MAST to the JET geometry

The groove speeds for the MAST geometry are more sensitive to free stream speed variations than the JET geometry. A comparison of the velocity field data between MAST and JET can be found in Table 4 and Fig. 8. The ND average groove speed is lower in the MAST geometry for all three cases (18%, 30% and 35% for the 3 m/s, 6 m/s and 10 m/s cases respectively). The RMS of the velocity fluctuations is higher for the 3 m/s and 6 m/s cases by 14% and 3%, while it is lower for the 10 m/s case (3%). The relative RMS values appear to be in general higher than the JET geometry by around 15–18%, while the breakup occurrences of the vortex are similar and marginally higher for the MAST geometry (2%, 3% and 3% for the 3 m/s, 6 m/s and 10 m/s cases respectively).

The MAST geometry exhibits lower speeds close to the side boundaries with the ND average velocity field being overall more uniform compared to the JET geometry. The RMS of the velocity fluctuations is also similar with the exception of a higher right corner RMS value for the 3 m/s case. The MAST and JET locational stability is not affected significantly by the free stream velocity changes. The locational stability of MAST is lower compared to JET.

Focusing on the entire section locational characteristics of each groove for both geometries (Fig. 12), the central grooves for MAST appear to form more locationaly stable vortices compared to the end grooves. This is not the case with the JET geometry at which all grooves appear to be more insensitive to end effects compared to the MAST geometry. A wake appears to form close to the top boundary of the grooves for the JET geometry for a significant amount of operational time of the device. The wake can occupy the free stream height by as much as 10–15%. Examining the locational stability of the grooves with a wake, no significant disruption is evident on the normal operation of the device. Moreover, the wake acts as a buffer zone which seems to be shielding the groove from free stream flow perturbations. On the contrary, the MAST geometry has no wake formation for all operating conditions. It is believed that any free stream perturbations are suppressed by the high shear stresses encountered inside the narrow free stream channel of the device. Evidences of instability suppression are also found in previous studies performed [27], where the MAST geometry appeared to behave more stably, when exposed to severe free stream perturbations.

4. Conclusions

A Particle Image Velocimetry (PIV) study of the flow field in HyperVapotrons was carried out to quantify the velocity field under isothermal conditions and reveal, in high spatial resolution (30 μm), the flow structures that are present and their locational stability inside the grooves of the flow geometry. The study considered two geometries (termed the JET and MAST variants from the Joint European Torus and Mega Amp Spherical Tokamak experiments respectively) under three operating conditions defined by the free stream speed enforced in each test section (3 m/s, 6 m/s and 10 m/s). A comparison was performed relative to the 6 m/s case as this is typical of operating conditions seen in the neutral beam systems at JET and MAST. The effects of the free stream channel speed on the groove flow structure characteristics were quantified.

The groove speeds for the MAST geometry are more sensitive to free stream speed changes compared to the JET geometry. Generally, the non-dimensional average groove speeds of MAST are lower and the relative values of the RMS of velocity fluctuations are higher compared to the JET geometry. This indicates that the vortex inside the MAST geometry is less stable and spinning at a lower speed. The vortex shape is similar for the two geometries. The MAST and JET vortex centroid locational stability seems to be insensitive to free stream velocity changes. The locational stability of the MAST vortex is overall lower compared to JET. A wake forms in the free stream at the top of the grooves inside the JET geometry. The wake does not affect significantly the vortex locational characteristics of the device, but might have an effect on the pumping loading of the device. The wake formation inside the MAST device is suppressed by the high shear stresses encountered in the free stream channel.

The flow in the grooves of the MAST geometry is affected significantly by end effects, while the JET geometry appears to be insensitive to them. As such, hydrodynamic end effects are likely to have an impact on the local thermal performance of the MAST geometry. Non-uniformities of the thermal loading performance and thermal tolerances of HHF components are extremely important and must be accounted for upon design and operation. It is not yet clear why the MAST geometry is susceptible to end effects. It can be speculated that the end effects are a result of the different boundary layer interaction between the local free stream and the grooves compared to the JET geometry. The difference in the boundary layer interaction processes between the JET and MAST is also evident by the presence and absence of wakes in the free stream channel consecutively as discussed earlier.

This study was performed under cold flow, isothermal conditions. These data are important as they provide evaluation benchmarks for future HV CFD analyses. However, the observed behaviour of the flow structures is expected to remain, at least qualitatively, during single phase heat transfer conditions. Therefore, the current results provide better understanding of the physics behind the Vapotron effect of the single phase heat transfer in the device before the vaporisation and ejection processes take place. The current velocity measurements can provide indicative values of the residence time of the liquid inside the grooves and therefore the ability to extract heat from the surrounding solid walls. Clearly, the single phase flow structures in the HV are heavily dependent on the device internal geometry. Looking ahead to the International Thermonuclear Experimental Reactor (ITER) and the Demonstration Power Plant (DEMO), it is likely that HVs will continue to be used as HHF components, so it is very important to understand the underlying HV behaviour in order to optimise engineering designs for other HHF applications not necessarily linked with fusion.

Future research will study the local flow field and associated structures within the grooves of the Hypervapotron geometries. In this way, the influence of single phase heat transfer on the currently detected behaviour of the flow structures can be evaluated. Most importantly, future work will also focus on the transition stages between single phase and two phase heat transfer coolant flow by quantifying the characteristic near the plasma facing wall which appears to play an important role in the heat transfer performance of local HV components (bottom of grooves and top of fins). The current study is the first step towards analysing and optimising the HV devices.

Acknowledgments

This work was funded by the RCUK Energy Program and EURATOM. The views and opinions expressed herein do not necessarily reflect those of the European Commission.

References

[1] H.D. Falter, E. Thompson, Performance of hypervapotron beam-stopping elements at JET, Fusion Technol. 29 (4) (1996) 584–598.
[2] F. Escourbiac, Experimental optimisation of a hypervapotron® concept for ITER plasma facing components, Fusion Eng. Des. 66–68 (2003) 301–304.
[3] J. Milnes et al., High heat flux (HHF) elements for negative ion systems on ITER, Fusion Eng. Des. 82 (5–14) (2007) 945–952.
[4] S. Pascalribot et al., 3D numerical simulations of hypervapotron cooling concept, Fusion Eng. Des. 82 (15–24) (2007) 1781–1785.
[5] G. Cattadori et al., Hypervapotron technique in subcooled flow boiling CHF, Exp. Therm. Fluid Sci. 7 (3) (1993) 230–240.
[6] J. Boscary, Dimensional analysis of critical heat flux in subcooled water flow under one-side heating conditions for fusion application, Fusion Eng. Des. 43 (2) (1998) 147–171.
[7] D. Youchison, M.U., Research and development task – engineering design activity final report – manufacturing and testing of permanent components – USA home Team, 1998: USA Home Team – ITER Report.
[8] A. Raffray, Critical heat flux analysis and R&D for the design of the ITER divertor, Fusion Eng. Des. 45 (4) (1999) 377–407.
[9] E. Di Pietro, The high heat flux components for ITER neutral beam system, Fusion Eng. Des. 49–50 (1–4) (2000) 177–182.
[10] C. Baxi, Thermal hydraulics of water cooled divertors, Fusion Eng. Des. 56–57 (2001) 195–198.
[11] K. Ezato, Critical heat flux test on saw-toothed fin duct under one-sided heating conditions, Fusion Eng. Des. 56–57 (2001) 291–295.
[12] V. Komarov, I. Labusov, A. Makhankov, Hypervapotron Analysis, St. Petersburg, Russia, 2001, pp. 1–62.
[13] M. Nightingale, The MAST neutral beam injection system, Fusion Eng. Des. 56–57 (2001) 529–532.
[14] R. Tivey, ITER R&D: vacuum vessel and in-vessel components: divertor cassette, Fusion Eng. Des. 55 (2–3) (2001) 219–229.
[15] V. Emetteur, A. Grosman, Critical Heat Flux Testing of Hypervapotron (2002) 1–15.
[16] S.H. Chang, W.-P. Baek, Understanding, predicting and enhancing critical heat flux, in: The 10th International Topical Meeting on Nuclear Reactor Thermal Hydraulics (NURETH-10), 2003: pp. 1–20.
[17] F. Escourbiac et al., A mature industrial solution for ITER divertor plasma facing components: hypervapotron cooling concept adapted to Tore Supra flat tile technology, Fusion Eng. Des. 75–79 (2005) 387–390.
[18] K. Ezato et al., Experimental examination of heat removal limitation of screw cooling tube at high pressure and temperature conditions, Fusion Eng. Des. 81 (1–7) (2006) 347–354.
[19] P. Chen, An experimental investigation of critical heat flux performance of Hypervapotron in subcooled boiling (2007).
[20] P. Chen, T.A. Newell, B.G. Jones, Heat transfer characteristics in subcooled flow boiling with hypervapotron, Annals Nucl. Energy 35 (6) (2008) 1159–1166.
[21] J.H. Bullock, D.L. Youchison, M.A. Ulrickson, A comparison of two-phase computational fluid dynamics codes applied to the ITER first wall hypervapotron, IEEE Trans. Plasma Sci. 38 (7) (2009) 1704–1708.
[22] J. Schlosser et al., Flat tile armour cooled by hypervapotron tube: a possible technology for ITER, Physica Scripta 81 (1) (2010). 011001-011001.
[23] J. Milnes, Computational modelling of the HyperVapotron cooling technique for nuclear fusion applications (2010).
[24] D.L. Youchison, Prediction of critical heat flux in water-cooled plasma facing components using computational fluid dynamics, Fusion Sci. Technol. 60 (July) (2011) 177–184.
[25] D.L. Youchison, Effects of hypervapotron geometry on thermalhydraulic performance, IEEE Trans. Plasma Sci. 40 (3) (2012) 653–658.
[26] J. Milnes et al., Hypervapotron design for the long pulse upgrades on MAST NBI, in: 20th IEEE/NPSS Symposium on Fusion Engineering, IEEE, San Diego, California, 2003.
[27] A. Sergis, Y. Hardalupas, T.R. Barrett, Potential for improvement in high heat flux HyperVapotron element performance using nanofluids, Nucl. Fusion 53 (11) (2013).